

DEVELOPMENT AND CALIBRATION OF A K-BAND GROUND-BASED HYPERSPSPECTRAL MICROWAVE RADIOMETER FOR WATER VAPOR MEASUREMENTS

Yan Xie*, Jingxiong Chen, Dawei Liu, Changchun Lv, Kai Liu, and Jungang Miao

School of Electronic and Information Engineering, Beihang University, No. 26, Xueyuan Road, Beijing 100191, China

Abstract—In this paper, a K-band ground-based hyperspectral microwave radiometer for atmospheric sounding is proposed, which improves the profile error and vertical resolution of moisture profiling under the high water vapor condition. The hyperspectral microwave radiometer (80 K-band spectral channels) can observe the rapidly changing weather with high sensitivity and accuracy of brightness temperature by using a stable high-speed receiver and an improved tipping calibration method. By combining several advantages of traditional microwave receiver, the MMIC receiver has good ultra-wideband performance, high linearity, and short measuring time. Moreover, through correcting the calibration parameters of traditional tipping calibration, the proposed calibration method can increase calibration accuracy based on the radiative transfer equation in the atmosphere. Measurement results demonstrate that the radiometer achieves a sensitivity of 0.1 K for 2 s of integration time and an accuracy of better than 0.77 K. For the water vapor profile, the variational retrievals method is used to extract the redundant information under the microwave hyperspectral condition. Preliminary comparisons of measured water vapor profiles with traditional results show good improvement of the profile error and vertical resolution.

1. INTRODUCTION

The technology of hyperspectral remote sensing in the infrared wavelength range has been developed in the pass decades. It allows the continuous frequency sampling of thousands narrow

Received 7 May 2013, Accepted 6 June 2013, Scheduled 10 June 2013

* Corresponding author: Yan Xie (xycrxyer@163.com).

bands in the atmospheric spectrum [1]. For example, the Infrared Atmospheric Sounding Interferometer, which is an 8461-channel infrared atmospheric sounder, was launched in 2006 for the hyperspectral measurements [2]. The applications of hyperspectral infrared technology for atmospheric sounding include the improvements of the meteorological parameters such as water vapor and temperature, which are important for short-term weather forecast [3].

With the development of microwave device technology, broad frequency bands could be multiplexed into a large number of spectral channels, and the hyperspectral microwave remote sensing can be realized. During the pass years, preliminary research on the combination of hyperspectral infrared and microwave for atmospheric profiles has been carried out [4]. Recently, Blackwell et al. in 2011 [5] presented that the airborne hyperspectral microwave radiometer could bring significantly improvement in accuracy and resolution of the retrieved atmospheric profile.

In this paper, the K-band ground-based hyperspectral microwave radiometer (BHU-K80) for water vapor profiling is introduced, which is used to measure the continuous atmospheric radiation spectral power in 18–26 GHz. The number of the spectral channels is 80. The BHU-K80 can observe the rapidly changing weather with high sensitivity and accuracy by using a stable high-speed receiver and an improved calibration method. By extracting the additional information from atmospheric hyperspectral microwave spectrum, the BHU-K80 not only reduces the profile error, but also improves the vertical resolution.

The microwave and millimeter-wave integrated circuit (MMIC) receiver is an important component of the BHU-K80. The architecture of superheterodyne receiver for traditional microwave radiometer can provide a higher gain because of the receiver gain is dispersed into several frequency bands [6–8]. And the receiver has a simple hardware architecture which can switch the receiver channel by changing the frequency of local oscillator. However, this kind of receiver increases the measuring time for whole frequency band. The multichannel direct-detection receiver for microwave radiometer provides high-speed measurement by measuring the multiple channels simultaneously [9–11]. However in this kind of design, the receiver array of 80 channels is required, which seriously increased the complexity of microwave radiometer system. The receiver of the BHU-K80 combined several advantages of traditional microwave radiometer [12–15] receiver. It is a single sideband superheterodyne receiver architecture, which divides the spectral channels continuously to reduce the complexity of the receiver. And then the multichannel direct-detection receiver

architecture divides the spectral channels simultaneously to reduce the measuring time of the receiver.

An improved tipping calibration method is used for the BHU-K80. In the traditional tipping calibration, the microwave radiometer uses the atmosphere itself as a cold calibration target. By measuring the brightness temperature of the sky at several elevation angles rapidly, the microwave radiometer can calculate an estimate of the system gain [16, 17]. However, the fluctuations of calibration parameters in different frequencies and different elevation angles are relatively large under hyperspectral microwave condition. Through correcting the calibration parameters of traditional tipping calibration based on the improved Liebe MPM model (1993) [18], the BHU-K80 can use an improved tipping calibration method to increase the calibration accuracy.

Variational retrievals method [19, 20] provides the preliminary retrieval of water vapor profiles from the BHU-K80. By comparing the performance of 80-channel and 4-channel or other channel numbers, it can be derived that the profile error and vertical resolution of the BHU-K80 are much better than traditional ground-based microwave radiometer. Due to the measured water vapor profiles with high vertical resolution, the monitoring of rapidly changing cloud can be achieved by hyperspectral microwave radiometer.

This paper will be organized as follows. Section 2 demonstrates the design strategies involved in the BHU-K80, which has short measuring time, low complexity architecture, and high sensitivity for 80 channels. Section 3 presents the calibration for the BHU-K80. The BHU-K80 uses an improved tipping calibration method to improve the calibration accuracy. An overview of accuracies of eighty channels is then provided. Section 4 next point out that the profile error and the vertical resolution of the BHU-K80 are improved for the water vapor profile. Finally, the suggestions for further research and development is summarized and provided in Section 5.

2. BHU-K80

2.1. System Architecture

Figure 1 shows a picture of the BHU-K80. The BHU-K80 is a ground-based hyperspectral microwave radiometer with eighty K-band frequency channels near the water vapor absorption line. Fig. 2 shows the frequency channels of the BHU-K80 and their corresponding bandwidths near 22.235 GHz. The water vapor resonances near 22 GHz are pressure broadened, and profiles can be obtained by measuring the intensity and shape of emission from pressure broadened lines [21].



Figure 1. The K-band ground-based hyperspectral microwave radiometer (BHU-K80) with 80 spectral channels.

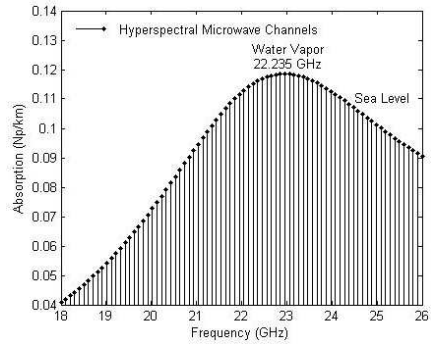


Figure 2. Eighty K-band channels of the BHU-K80.

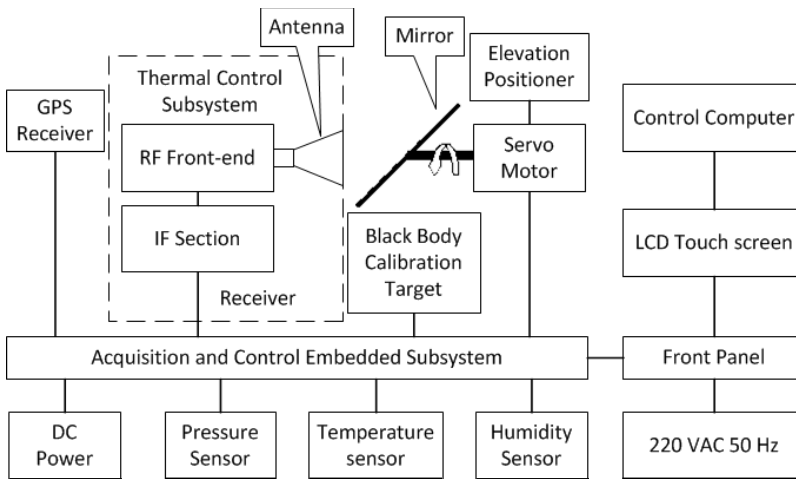


Figure 3. Block diagram of the BHU-K80 system.

The frequency channel near 22 GHz is appropriate for ground based profiling in relatively moist areas.

The BHU-K80 uses a horn antenna to provide a half-power beamwidth of 10 degrees, and K-band is evenly divided into 80 frequency channels by a multichannel receiver. By measuring the noise power of each channel, the system provides the power spectra of atmospheric radiation in the range of 18–26 GHz. The block diagram in Fig. 3 provides an overview of the primary system level components in the BHU-K80.

The atmospheric microwave signal is reflected to the antenna via a rotatable flat mirror, which is driven by the servo motor. When the flat mirror points to the black body calibration target, BHU-K80 starts the calibration process. Meanwhile, the temperature sensor acquires and transmits the physical temperature of the black body calibration target to the acquisition and control embedded subsystem. Moreover, the GPS receiver supplies latitude and longitude data of the radiometer system. And the pressure sensor and humidity sensor supplies real-time surface meteorological data for atmospheric profiles retrieval.

2.2. Antenna

Incoming microwave energy from different angles passes through the atmosphere and is reflected by the 45° flat mirror into the antenna. The BHU-K80 uses a conical horn antenna with ultra-wideband, high directivity, narrow beamwidth, high main-beam efficiency, high radiation efficiency, low side lobe levels and simple structure [22]. As shown in Fig. 4, the ultra-wideband antenna has a bandwidth of 36% (18–26 GHz), circular polarization, and a VSWR of 1.4, 1.8, and 1.6 at the radiometer typical operating frequencies, respectively. The performance of the antenna demonstrating the beamwidth of $10\text{--}14^\circ$, gain of 19–25 dB, side lobe of less than 20 dB, and back lobe of less than 30 dB over the radiometer's frequency range.

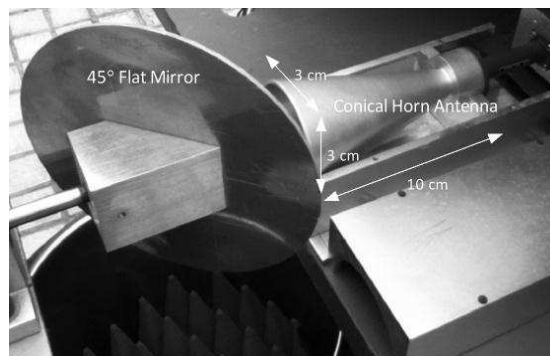


Figure 4. Conical horn antenna and 45° flat mirror of the BHU-K80.

The size of the ultra-wideband antenna is only $10\text{ cm} \times 3\text{ cm} \times 3\text{ cm}$, with a waveguide flange as the radio frequency (RF) port, which is a circular-rectangular waveguide transition that bridges the K-band receiver for operation from 18–26 GHz. The measured performances of the proposed ultra-wideband antenna for the BHU-K80 are summarized in Table 1.

Table 1. Antenna characteristic.

Typical Frequency		18 GHz	22 GHz	26 GHz
3-dB Beamwidth	<i>E</i> -Plane	13.8°	11.2°	10°
	<i>H</i> -Plane	14°	12.9°	11.8°
Gain	<i>E</i> -Plane	19.7 dB	20 dB	23.4 dB
	<i>H</i> -Plane	18.7 dB	20.5 dB	24.7 dB
Side Lobes	<i>E</i> -Plane	-20 dB	-26 dB	-25 dB
	<i>H</i> -Plane	-28 dB	-30 dB	-28 dB
Back Lobes	<i>E</i> -Plane	-35 dB	-51 dB	-48 dB
	<i>H</i> -Plane	-32 dB	-37 dB	-36 dB
VSWR		1.4	1.8	1.6

The servo motor can rotate the 45° flat mirror to point the beam to any elevation angle in 360°, which is recorded by elevation positioner. The antenna beam points to the sky, and the black body calibration target when elevation angle pointed 0–180°, 270°, respectively.

2.3. Receiver

An ultra-wideband, 18–26 GHz, eighty spectral channel receiver based on MMIC technology for the BHU-K80 has been designed and fabricated. To achieve more spectral channels, short measuring time and low complexity, the improved superheterodyne architecture is used as shown in Fig. 5. BHU-K80 is designed to verify the improvements of atmospheric profiles under microwave hyperspectral condition. For

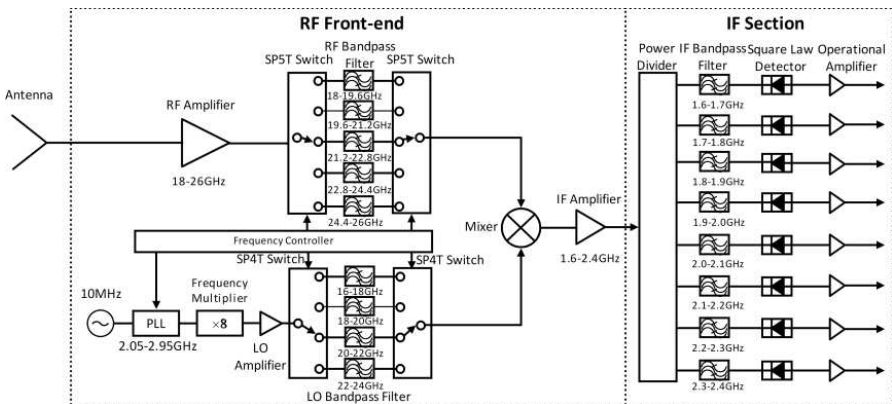


Figure 5. Block diagram of the proposed 80 channels receiver for hyperspectral microwave radiometer.

this purpose, receiver with eighty spectral channels is proposed, which is easy to implement. Eighty (receiver spectral channels) is ten (radio frequency spectral channels) multiplied by eight (intermediate frequency spectral channels). The number of spectral channels can be easily increased with the proposed architecture. By using more spectral channels, the profile error and vertical resolution of atmosphere can be further improved. In the future, the hyperspectral microwave radiometer may have thousands of spectral channels, as in the infrared wavelength range.

The proposed receiver consists of an RF front-end and an intermediate frequency (IF) section.

The RF front-end is implemented in the single sideband (SSB) superheterodyne architecture to obtain the first spectral channel selection at 18–26 GHz frequency. The input signal at 18–26 GHz is amplified and then ten RF bands, 18–18.8 GHz, 18.8–19.6 GHz, 19.6–20.4 GHz, 20.4–21.2 GHz, 21.2–22 GHz, 22–22.8 GHz, 22.8–23.6 GHz, 23.6–24.4 GHz, 24.4–25.2 GHz, 25.2–26 GHz, are down-converted to an IF of 1.6–2.4 GHz with different local oscillator (LO) frequencies. The high-intermediate frequency (IF) allows us to obtain image rejection of as large as 60 dB by the RF bandpass filter [23–25]. Each RF bandpass filter is shared by two adjacent RF bands to reduce the complexity of the RF front-end.

Then IF section adopts the multichannel direct-detection architecture to obtain the selectivity of better than 0.5% in 100 MHz bandwidth without K-band filters. Following the mixer and IF amplifier of RF front-end, a 1/8 Wilkinson power divider [26–28] at 1.6–2.4 GHz and a bank of IF bandpass filters enable the simultaneous measurements at the eight IF bands: 1.6–1.7 GHz, 1.7–1.8 GHz, 1.8–1.9 GHz, 1.9–2.0 GHz, 2.1–2.2 GHz, 2.2–2.3 GHz, and 2.3–2.4 GHz. And then, signals are input to eight diode square law detectors, which generate the voltage proportional to the input microwave signal power [29].

When the receiver is switched on, frequency controller of the RF front-end immediately selects the correct RF bandpass filter and LO frequency by controlling switches and phase locked loop (PLL). Through the appropriate configuration, the RF signal at 18–26 GHz is divided into 80 spectral channels with 100 MHz bandwidth. Typical frequency channels with different LO frequencies and filters are shown in Table 2.

The 16.4–23.6 GHz LO frequency is multiple through a 2.05–2.95 GHz PLL with the sweep time less than 100 ns, and then the LO signal will be amplified through a LO amplifier. In this design, four microstrip LO bandpass filters are added before the mixer to have

Table 2. Typical frequency channels.

RF Bandpass Filter	LO Frequency	IF Bandpass Filter	Typical Channels
18.0–19.6 GHz	16.4 GHz	1.6–1.7 GHz	18.0–18.1 GHz
18.0–19.6 GHz	16.4 GHz	1.7–1.8 GHz	18.1–18.2 GHz
18.0–19.6 GHz	16.4 GHz	1.8–1.9 GHz	18.2–18.3 GHz
18.0–19.6 GHz	16.4 GHz	1.9–2.0 GHz	18.3–18.4 GHz
18.0–19.6 GHz	16.4 GHz	2.0–2.1 GHz	18.4–18.5 GHz
18.0–19.6 GHz	16.4 GHz	2.1–2.2 GHz	18.5–18.6 GHz
18.0–19.6 GHz	16.4 GHz	2.2–2.3 GHz	18.6–18.7 GHz
18.0–19.6 GHz	16.4 GHz	2.3–2.4 GHz	18.7–18.8 GHz
18.0–19.6 GHz	17.2 GHz	2.3–2.4 GHz	19.5–19.6 GHz
19.6–21.2 GHz	18.0 GHz	2.3–2.4 GHz	20.3–20.4 GHz
19.6–21.2 GHz	18.8 GHz	2.3–2.4 GHz	21.1–21.2 GHz
21.2–22.8 GHz	19.6 GHz	2.3–2.4 GHz	21.9–22.0 GHz
21.2–22.8 GHz	20.4 GHz	2.3–2.4 GHz	22.7–22.8 GHz
22.8–24.4 GHz	21.2 GHz	2.3–2.4 GHz	23.5–23.6 GHz
22.8–24.4 GHz	22.0 GHz	2.3–2.4 GHz	24.3–24.4 GHz
24.4–26.0 GHz	22.8 GHz	2.3–2.4 GHz	25.1–25.2 GHz
24.4–26.0 GHz	23.6 GHz	2.3–2.4 GHz	25.9–26.0 GHz

immunity to the harmonic frequency above 2 GHz.

The advantages of MMIC technology can be summarized as small mechanical size, high electrical reliability, good thermal stability, excellent electromagnetic shielding, and low manufacturing costs [30, 31]. To have immunity to the shell-and-tube package parasitic parameters of active device, the operating frequency and bandwidth are greatly increased. Based on MMIC technology, ultra-wideband chips of K-band low noise amplifiers (LNAs), mixer and switches were designed for the RF front-end of the BHU-K80, as shown in Fig. 6. This highly integrated RF front-end not only reduces the size of the BHU-K80, but also improves its thermal stability since all of the RF circuits are housed in a small box. Due to the good thermal conductivity of K-band LNAs, the gain fluctuation of RF section can be reduced, which will be explained in Section 2.4.

These K-band chips were made from Wuxi Huace Electronic Systems Ltd. The K-band LNAs are used for the RF amplification of the radiometer and have a major impact on the system

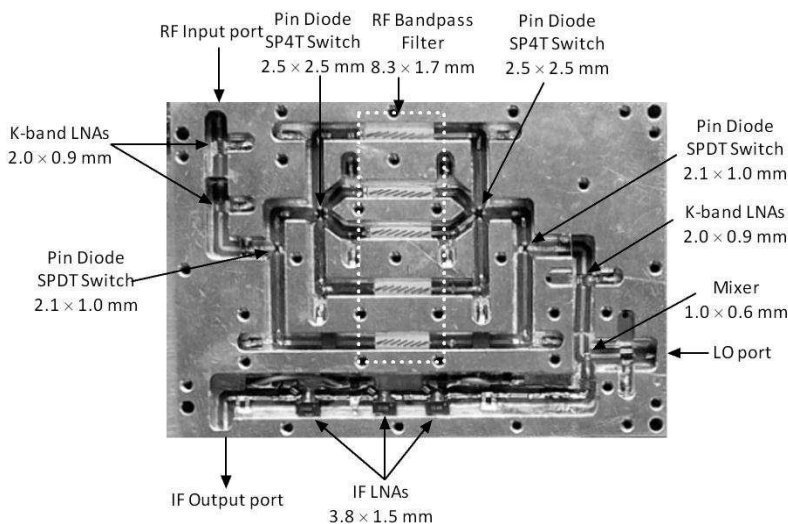


Figure 6. Illustration of the highly integrated RF front-end of the BHU-K80.

temperature [32]. It provides 16 dB of gain and a 2.4 dB average noise figure with a single positive supply of +5 V in the 18–26 GHz frequency range. Following the K-band LNAs are pin diode switches, with a switching time of 15 ms maximum and an insertion loss of 0.8 dB. The microstrip coupled line bandpass filters of RF front-end achieve an approximate bandwidth of 7%, a loss flatness of 0.2 dB, and an insertion loss of 1.5 dB. The passive double balanced mixer was used for RF front-end, with a conversion loss of 10–13 dB at 18–26 GHz. A 16.4–23.6 GHz LO signal is injected into this mixer through the LO port to generate the IF signals.

Using the designed receiver architecture in this Section, the ultra-wideband multichannel RF front-end is fabricated as shown in Fig. 7. The size of RF front-end including RF circuit, frequency controller, coaxial line, waveguide coaxial connector, and metal shield box is 24 cm × 20 cm.

As illustrated in Fig. 8, the direct-detection linear IF section was placed in the thermal control subsystem. RF front-end was also placed in the same thermal control subsystem with a maximum variability of 0.1 K. During the operations in outdoor condition, measurement results show that the receiver has a stable temperature of 5°C.

Figure 9 presents the measured power gain (PG), image rejection ratio (IRR), and noise figure (NF) performance of the receiver. On the horizontal axis, the frequency is defined as the designed ten RF bands in this Section, which is divided by the RF front-end. The wide-band

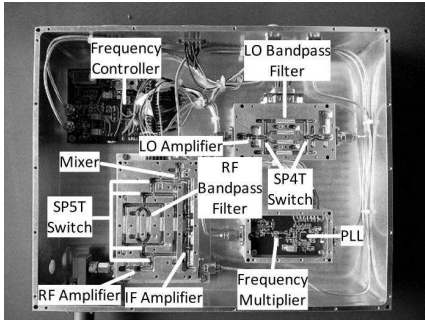


Figure 7. Photograph of the fabricated RF front-end.

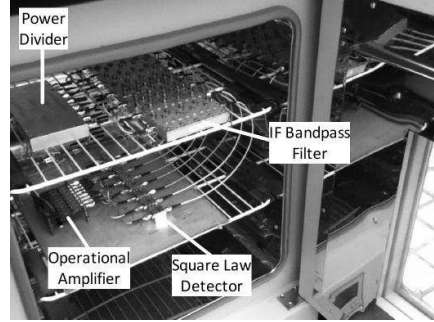


Figure 8. Photograph of the IF section in the thermal control subsystem.

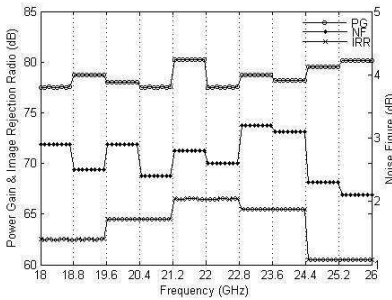


Figure 9. Measured power gain (PG), image rejection ratio (IRR), and noise figure (NF) of eighty receiver channels.

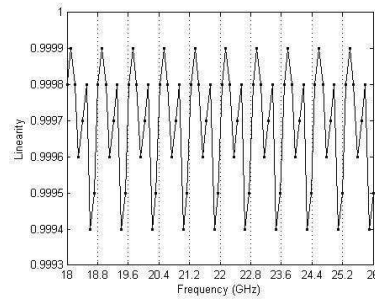


Figure 10. Measured linearity performance of receiver with eighty channels.

performance of the receiver demonstrating a measured average gain of 79 dB, an average noise figure of 2.6 dB, and an image rejection ratio greater than 60 dB over the specified 2–18 GHz frequency range could be obviously obtained from these results.

In Fig. 10 the linearity relation between the output voltage and the microwave signal power are presented as a curve of all the 80 receiver channels, it can be seen that the minimum linearity achieves 0.9994 at 18–26 GHz. Considering that the square law detector produces a voltage proportional to the input microwave power, the linearity mainly depends on the eight square law detectors in IF section and RF front-end has little influence on this parameter. So the curve is periodic with a period of eight different values, which is different from other parameters.

To observe the rapid weather changes of the atmospheric

environment, the measuring time of the eighty channel receiver was considered. For this purpose, the measuring time and brightness temperatures were measured by the BHU-K80. For the observation performed at 15:18 Beijing time on September 02, 2011, the measuring time achieved a maximum value of 188 μ s and brightness temperatures had a range of 20–65 K at 18–26 GHz. The BHU-K80 scanned the 180° sky with angular resolution of 0.1°, and it would spend 0.34 seconds in the whole scanning process with multichannel measuring time of 200 μ s. It is an appropriate time for hyperspectral microwave radiometer to observe the rapid weather changes.

2.4. Sensitivity of the BHU-K80

The BHU-K80 was simplified to a linear system, which expressed as an ideal RF front-end with equivalent noise temperature, as shown in Fig. 11. Parameters T_A and T_{REC} represent the antenna temperature and the receiver noise temperature, respectively. B and τ represent the bandwidth of single channel and integration time, respectively. G_0 and C_d represent power gain of the RF front-end and IF section, and k is Boltzmann constant.

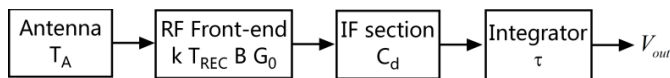


Figure 11. Block diagram of the total power microwave radiometer.

After the RF Front-end, each signal is input to IF section that produces a voltage proportional to the signal power at the output of the RF Front-end. The radiometer output voltage (V_{out}) is given as:

$$V_{out} = kBG_0C_d(T_A + T_{REC}) \tag{1}$$

From (1), the radiometer system temperature fluctuations ($\Delta(T_A + T_{REC})$) and gain fluctuation ($\Delta G/G$) will contribute to the output fluctuation. The sensitivity of a total power radiometer, which is termed the “temperature resolution”, is given as [33]:

$$\Delta T = (T_A + T_{REC}) \sqrt{\frac{1}{B\tau} + \left(\frac{\Delta G}{G}\right)^2} \tag{2}$$

The BHU-K80 is a hyperspectral microwave radiometer with 80 K-band channels, and the bandwidth (B) of each channel is 40 MHz. From (2), BHU-K80 need a lower gain fluctuation ($\Delta G/G$) than traditional microwave radiometer. For this purpose, the antenna and receiver were placed in thermal control subsystem of the BHU-K80, as

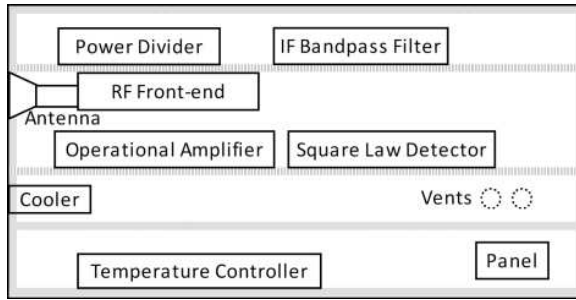


Figure 12. Illustration of thermal control subsystem of the BHU-K80.

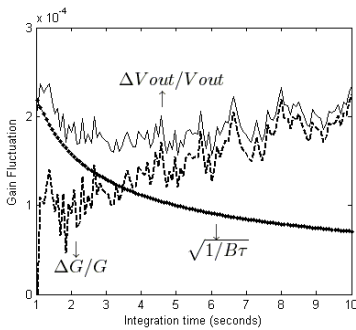


Figure 13. Measured gain fluctuation of the receiver in thermal control subsystem.

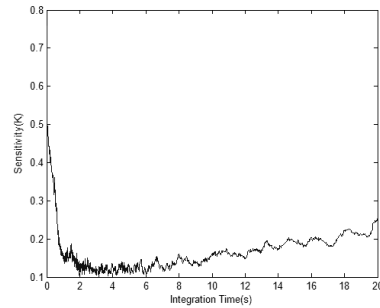


Figure 14. Sensitivity of the BHU-K80.

shown in Fig. 12. The cool wind generated by the cooler is discharged upward through the cavity, and then is sucked into the vents. After continuous loop, the temperature stability of the cavity reaches a maximum variability of 0.1 K.

The gain fluctuation ($\Delta G/G$), which is independently determined by measuring the fluctuation of radiometer output voltage ($\Delta V_{out}/V_{out}$), is given as:

$$\frac{\Delta G}{G} = \sqrt{\left(\frac{\Delta V_{out}}{V_{out}}\right)^2 - \frac{1}{B\tau}} \tag{3}$$

The RF Front-end and the IF section, which provide 77–80 dB of the power gain, exhibit a gain fluctuation ($\Delta G/G$) of about 5×10^{-5} – 1×10^{-4} with the integration time of 2 seconds, as shown in Fig. 13. These results show good gain stability in the receiver system, which is important for determining the sensitivity of the BHU-K80, as explained in (2).

The BHU-K80 uses the Allan variance to describe the sensitivity because it is convergent with the noise of receiver gain fluctuation. Total measured brightness temperatures are divided into M groups of τ seconds each, and the Allan variance is one half of the mean square error between contiguous averages brightness temperature (T_i). Allan variance is calculated as [34]:

$$\Delta T^2 = \frac{1}{2M} \sum_{i=1}^{M-1} [T_{i+1}(\tau) - T_i(\tau)]^2 \quad (4)$$

The mean sensitivity of the hyperspectral microwave radiometer is 0.1–0.2 K with the integration time of 2 seconds, as shown in Fig. 14.

3. CALIBRATION

Since the zenith brightness temperature in the K-band are generally less than 50 K under clear sky, K-band microwave radiometer can be calibrated using the tipping calibration. In this calibration method, the microwave radiometer uses the atmosphere itself as a cold calibration target. By measuring the brightness temperature of the sky at several elevation angles rapidly, the microwave radiometer can calculate an estimate of the zenith brightness temperature based on the radiative transfer equation in the atmosphere.

Through correcting the calibration parameters of traditional tipping calibration under the microwave hyperspectral condition, the BHU-K80 can use an improved tipping calibration method to improve the calibration accuracy. The corrected calibration parameters are calculated by the atmospheric profile data, which were published by Beijing Meteorological Bureau in the last two decades.

3.1. Basic Theory

Tipping calibration method is based on the following principle: in the clear sky conditions, atmospheric opacity of each direction can be normalized to the same opacity directed toward zenith. By ignoring the radiation bending caused by the refractive index gradient in plane stratified atmosphere, the opacity is given as [17]:

$$\tau(\theta) = \tau(90^\circ) / \sin(\theta) \quad (5)$$

where the angle θ is the observation direction of microwave radiometer, and $\tau(90^\circ)$ is the opacity at the zenith. The brightness temperature can be estimated by the radiative transfer equation through the atmosphere in the Rayleigh-Jeans approximation [35]:

$$T_b(\theta) = T_{bg} e^{-\tau(\theta)} + T_m [1 - e^{-\tau(\theta)}] \quad (6)$$

where T_b , T_m , T_{bg} are the atmospheric brightness temperature, mean radiating temperature, and cosmic background brightness temperature ($T_{bg} = 2.75$ K), respectively.

Due to the finite antenna beamwidth, the antenna temperature T_A would be higher than the atmospheric brightness temperature T_b . The error of antenna temperature δT_A is experimentally obtained by the formula [17]:

$$\delta T_A(\theta) = \frac{\sigma^2}{16 \ln(2)} (T_m - T_{bg}) e^{-\tau(\theta)} [2 + (2 - \tau(\theta)) t g^{-2}(\theta)] \tau(\theta) \quad (7)$$

where σ is the 3-dB beamwidth of antenna (in radians). The error of antenna temperature increases by increasing the beamwidth of antenna. So it is necessary to correct the atmospheric brightness temperature using the equation [16]:

$$T_b(\theta) = T_A(\theta) - \delta T_A(\theta) \quad (8)$$

With the brightness temperatures $T_b(\theta)$ measured in different directions, the opacity can be expressed as [36]:

$$\tau(\theta) = \ln \left(\frac{T_m - T_{bg}}{T_m - T_b(\theta)} \right) \quad (9)$$

In the calibration process, BHU-K80 measures the atmospheric brightness temperature of nine angles of 19.35° , 23.4° , 30.15° , 41.85° ,

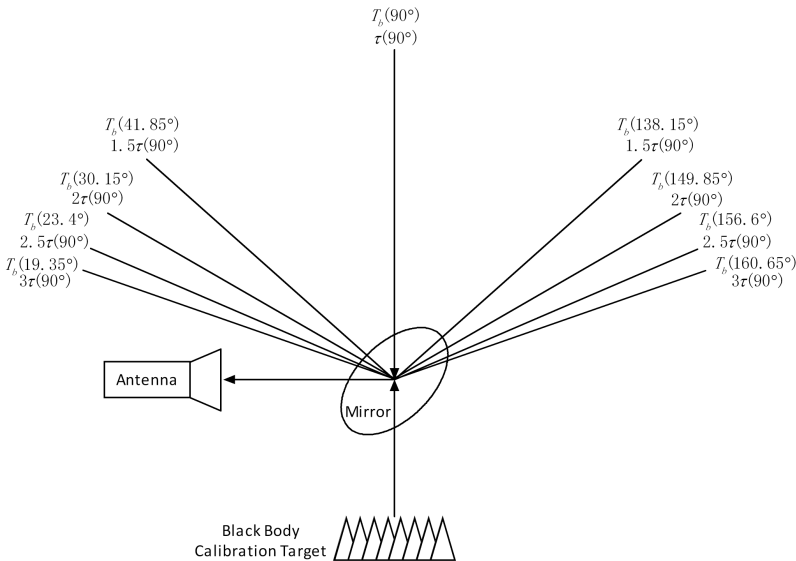


Figure 15. Typical elevation angle in the tipping calibration process of the BHU-K80.

90°, 138.15°, 149.85°, 156.6°, and 160.65°, as shown in Fig. 15. The mirror points to the black body calibration target with the angle of 270°.

The atmospheric brightness temperatures measured by BHU-K80 can be described as follow:

$$T_b(\theta) = rG_{sys} [V_b(\theta) - V_{ref}] + T_{ref} \tag{10}$$

where T_{ref} and V_{ref} are the brightness temperature and radiometer output voltage of the black body calibration target, and V_b , G_{sys} , r are the radiometer output voltage of sky, gain of radiometer system, and gain calibration coefficient, respectively. By using an iterative algorithm to adjust the gain calibration coefficient close to 1, gain of radiometer system is then calculated.

3.2. Improvements

In the traditional tipping calibration method, mean radiating temperature is substituted into (9) as a constant parameter. For the hyperspectral microwave radiometer, which has an ultra-wideband of 8 GHz and eighty spectral channels, mean radiating temperature fluctuations are greater than 2 K in different frequencies and different elevation angles. Fig. 16 shows how the mean radiating temperature uncertainties affect the calibrations of BHU-K80, which is calculated by formula (9). The atmospheric state for this simulation has a mean radiating temperature of 270 K and a zenith brightness temperature of 51.2 K. From Fig. 16, we see that the mean radiating temperature uncertainties can cause great calibration errors when low elevation angles are used under microwave hyperspectral condition.

To achieve high calibration accuracy, mean radiating temperatures are corrected by the profiling data from Beijing Meteorological Bureau

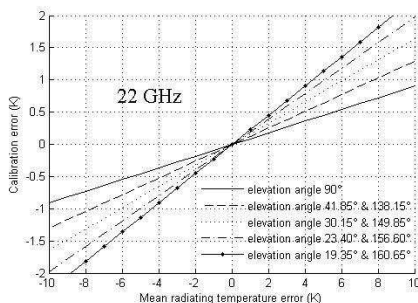


Figure 16. The calibration error and the mean radiating temperatures error with different elevation angles.

with each month in the last two decades. According to the radiative transfer equation, the mean radiating temperature can be given as [17]:

$$T_{m,f}(\theta) = \int_0^\infty T'_f e^{-\tau_f(\theta)} d\tau_f(\theta) / \left(1 - e^{-\tau_f(\infty,\theta)}\right) \quad (11)$$

where f is frequencies of eighty K-band spectral channels.

The first term T'_f from (11), is a temporary parameter define as [18]:

$$T'_f = \frac{B_f(t)c^2}{2f^2k} \quad (12)$$

$$B_f(t) = \frac{2hf^3}{c^2} \cdot \frac{1}{\exp\left(\frac{hf}{kt}\right) - 1} \quad (13)$$

where h , k , and c are Planck constant, Boltzmann constant, and vacuum speed of light, respectively. And t is the atmospheric temperature under the current altitude, which is extracted from the data of Beijing atmospheric temperature profiles.

The second term $\tau_f(\theta)$ from (11) is given as [18]:

$$\tau_f(\theta) = \int_0^{h_z} K_a(z) \sec \theta dz \quad (14)$$

where z and h_z are the direction of antenna beam and corresponding height of the stratosphere. And K_a is atmosphere absorbance, which is approximated by the linear spectral lines of oxygen and water vapor based on the improved Liebe MPM model (1993):

$$K_a(f) = 0.1820fN''(f) \quad (15)$$

where $N''(f)$ is the complex refractive of atmosphere. Under the cloud free and clear sky conditions, the complex refractive index of atmosphere mainly includes the contribution of the 44 oxygen spectral lines and 34 water vapor spectral lines. $N''(f)$ can be calculated as follows:

$$N''(f) = \sum_{i=1}^{44} S_i F(f)_i + \sum_{j=1}^{34} S_j F(f)_j \quad (16)$$

where S_i is the line strength (kHz) and $F(f)_i$ the complex shape function (GHz^{-1}). The contribution of the oxygen absorption spectrum can be expressed as:

$$S_i = 10^{-6} a_1 p \theta^3 \exp[a_2(1 - \theta_i)] \quad (17)$$

$$F(f)_i = \frac{f}{f_i} \left[\frac{1 - i\delta_i}{f_i - f - i\gamma_i} - \frac{1 + i\delta_i}{f_i + f + i\gamma_i} \right] \quad (18)$$

where

$$\gamma_i = 10^{-3} a_3 \left(p\theta_t^{(0.8-a_4)} + 1.1e\theta_t \right) \tag{19}$$

$$\delta_i = 10^{-3} (a_5 + a_6\theta_t) p\theta_t^{0.8} \tag{20}$$

$$\theta_t = 300 / (t + 273.15) \tag{21}$$

The contribution of the water vapor absorption spectrum can be expressed as:

$$S_j = 10^{-3} b_1 e\theta_t^{3.5} \exp[b_2(1 - \theta_t)] \tag{22}$$

$$F(f)_j = \frac{f}{f_j} \left[\frac{1 - i\delta_j}{f_j - f - i\gamma_j} - \frac{1 + i\delta_j}{f_j + f + i\gamma_j} \right] \tag{23}$$

where

$$\gamma_j = 10^{-3} b_3 \left(p\theta_t^{b_4} + b_5 e\theta_t^{b_6} \right) \tag{24}$$

$$\delta_j = 0 \tag{25}$$

From (17)–(25), p , t , and e are the pressure, temperature, vapor pressure under the current altitude, respectively. These parameters are based on the pressure profiles, temperature profiles, and vapor pressure profiles of Beijing meteorological data in the past. Constants $a_1 - a_6$ and $b_1 - b_6$ are the spectral absorption efficiency of oxygen and water vapor.

In summary, the mean radiating temperature can be corrected by the profiles from Beijing Meteorological Bureau with 80 K-band spectral channels and 180° observation angle. The profile data are divided into 12 month, and the BHU-K80 should be recalibrated every month to ensure the highest accuracy.

3.3. Accuracy of the BHU-K80

To estimate the effects of the mean radiating temperature uncertainties, we simulated tipping calibrations using atmospheric profile data from Beijing Meteorological Bureau. The calibration errors with zenith elevation angle are shown in Table 3 (row 2–3), which suggests that the use of improved Liebe MPM model can significantly improve the calibration accuracy under microwave hyperspectral condition.

The system random noise would also affect the calibration errors. To see its influence on the absolute accuracy of BHU-K80, we simulated a tipping calibrations process with measured system random noise of BHU-K80. The results with zenith elevation angles are summarized in Table 3 (row 4). The calibration errors arise from system random noise are about 0.3 to 0.5 K.

Table 3. Calibration errors arise from mean radiating temperature and system random noise.

		Frequency	18 GHz	20 GHz	22 GHz	24 GHz	26 GHz
Calibration errors	Mean radiating temperature	Basic T_m	0.47 K	0.49 K	0.66 K	0.57 K	0.45 K
		Improved T_m	0.14 K	0.17 K	0.23 K	0.17 K	0.15 K
	System random noise (Sensitivity of BHU-K80)		0.38 K	0.53 K	0.44 K	0.38 K	0.49 K

For comparison of brightness temperature measured by the BHU-K80 with brightness temperature provided by Beijing Meteorological Bureau, measurements were performed at Beihang University during August 30, 2011. The BHU-K80 was pre-calibrated with basic calibration data and improved calibration data, under the surface temperature of 32.11°C and the surface atmospheric pressure of 99776 Pa conditions. The calibration errors of the zenith brightness temperatures are shown in Fig. 17.

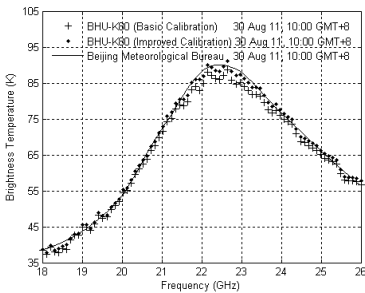


Figure 17. Measured brightness temperature comparison between Beijing Meteorological Bureau and the BHU-K80 with basic and improved calibrations.

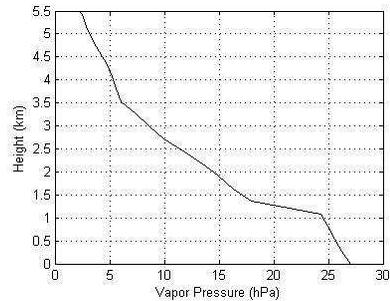


Figure 18. Measured vapor pressure profiles during the September 2, 2011.

The brightness temperature spectral lines showed a consistent trend in the whole K-band. The absolute calibration error of basic tipping calibration was 1.55 K, and it reduced to 0.77 K by applying the improved tipping calibration. Based on the improved tipping calibration for BHU-K80, accuracies of eighty channels could achieve better than 0.8 K at 18–26 GHz.

The specifications of the hyperspectral microwave radiometer are summarized in Table 4. Considering that the BHU-K80 is a complete microwave radiometer, its sensitivity and calibration accuracy are similar to the previous K-band ground-based microwave radiometers. Under this condition, it can achieve higher profile accuracy with more spectral channels, which will be explained in Section 4. The next plan is to increase the spectral channels to 512 to achieve a future hyperspectral microwave radiometer (BHU-K512).

Table 4. Specifications of the similar ground-based K-band microwave radiometers.

Parameter	Specifications		
Name of radiometer	BHU-K80	MP1500A	RPG-HUMPRO
Frequency range	18–26 GHz	22–30 GHz	22.24–31.4 GHz
Spectral channels	80 channels	21 channels	7 channels
Channel bandwidth	100 MHz	300 MHz	230 MHz
Calibration accuracy	0.8 K	< 1 K	0.5 K
Sensitivity	0.1–0.2 K	0.1–1 K	0.1 K
Integration time	2–6 seconds	0.01–2.5 seconds	1 seconds

4. PRELIMINARY PROFILE MEASUREMENTS

The BHU-K80 adopts a variational retrievals method for the profile retrievals, which provide an optimal method of combining observations with a background. This method was suggested by Levenberg and Marquardt to deal with nonlinear problems. The iteration method is performed as below [19]:

$$J(x) = [x - x^b]^T B^{-1} [x - x^b] + [y - H(x)]^T R^{-1} [y - H(x)] \quad (26)$$

where y and x^b are the observation vector and background vector; R and B are the error covariance of observation and background, respectively; $H(x)$ is the forward model operator.

The observation error covariance (R) has contributions from the measured sensitivity (0.1–0.2 K) and accuracy (0.2–0.8 K) of the BHU-K80, as shown in Figs. 14 and 17. During the September 2, 2011, measurements were performed at Beihang University for preliminary comparison of profiles measured by 80 channels with 4 channels. Fig. 18 shows vapor pressure profile degrades with height, from 27 hPa near the surface, approximately linearly from 1–5.5 km.

Profile error is an important aspect of the retrieval's performance. It is possible to estimate the profile error by assuming that the observations and background are Gaussian and uncorrelated. In this case, Rodgers (2000) shows that the covariance of the profile error is a simple function of the observations and background error covariance [20]:

$$A = (H^T R^{-1} H + B^{-1})^{-1} \quad (27)$$

The profile error of vapor pressure is plotted in Fig. 19. This shows the errors in the vapor pressure retrieved by the BHU-K80 is expected to approach 1 hPa near the surface, but varies with height, to exceed 1.5 hPa near 5 km. For comparison of 4 channels with 80 channels, the vapor pressure error improves from 3.2 hPa to 2.7 hPa near 2.5 km.

Moreover, vertical resolution is another important aspect of the retrieval's performance. Rodgers (2000) defines the vertical resolution (Δz) as the reciprocal of the diagonal of the averaging kernel matrix [20]:

$$\Delta z = \delta z / \text{diag}(AH^T R^{-1} H) \quad (28)$$

where δz is the level spacing. Δz is evaluated in Fig. 20, which shows that the vertical resolution of vapor pressure profiles varies with height, from 1 km near the surface, approximately 3 km near the 5 km. For comparison of 4 channels with 80 channels, the vertical resolution of vapor pressure profile improves from 5 km to 3.1 km near 2.5 km.

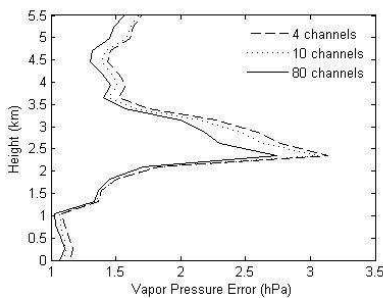


Figure 19. Error analysis for vapor pressure profile with different channel numbers.

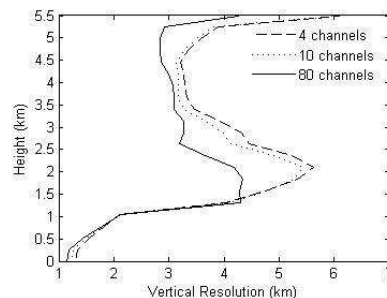


Figure 20. Vertical resolution analysis for vapor pressure profile with different channel numbers.

5. CONCLUSION

In this paper, a K-band ground-based hyperspectral microwave radiometer is presented. By combining the architecture of superheterodyne and multichannel direct-detection of traditional microwave radiometer receiver, the proposed microwave receiver has advantages of excellent multichannel measuring time, good wideband performance, high-linearity, and low complexity. Moreover, the proposed tipping calibration method can significantly improve the calibration accuracy under the microwave hyperspectral condition. With 8 GHz RF bandwidth, a sensitivity of 0.1 K for 2 s of integration time and an accuracy of better than 0.77 K, the BHU-K80 can achieve optimum performance at K-band operating frequencies. From these measurement results, the proposed radiometer noise is suitable for K-band ground-based hyperspectral microwave radiometer applications. Preliminary measurements of water vapor profiles show good improvement of the profile error and vertical resolution.

REFERENCES

1. Smith, W. L., "Atmospheric soundings from satellites — False expectation or the key to improved weather prediction?," *Q. J. R. Meteorol. Soc.*, Vol. 117, No. 498, 267–297, Jan. 1991.
2. Chalon, G., F. Cayla, and D. Diebel, "IASI: An advanced sounder for operational meteorology," *Proc. 52nd Congr. IAF*, 1–5, Oct. 2001.
3. Smith, W. L., H. Revercomb, G. Bingham, A. Larar, H. Huang, D. Zhou, J. Li, X. Liu, and S. Kireev, "Evolution, current capabilities, and future advance in satellite nadir viewing ultra-spectral IR sounding of the lower atmosphere," *Atmos. Chem. Phys.*, Vol. 9, No. 15, 5563–5574, 2009.
4. Blackwell, W. J., et al., "Combined microwave and hyperspectral infrared retrievals of atmospheric profiles in the presence of clouds using nonlinear stochastic methods," *Geoscience and Remote Sensing Symposium (IGARSS)*, 2814–2817, Barcelona, Spain, Jul. 2007.
5. Blackwell, W. J., et al., "Hyperspectral microwave atmospheric sounding," *IEEE Trans. on Geosci. Remote Sens.*, Vol. 49, No. 1, 128–142, Jan. 2011.
6. Hotopan, G. R., S. Ver-Hoeye, C. Vazquez-Antuna, R. Cambor-Diaz, M. Fernandez-Garcia, F. Las Heras Andres, P. Alvarez, and R. Menéndez, "Millimeter wave microstrip mixer based on

- graphene,” *Progress In Electromagnetics Research*, Vol. 118, 57–69, 2011.
7. Guo, J., Z. Xu, C. Qian, and W.-B. Dou, “Design of a microstrip balanced mixer for satellite communication,” *Progress In Electromagnetics Research*, Vol. 115, 289–301, 2011.
 8. Wan, Q. and C. Wang, “A wideband CMOS current-mode down-conversion mixer for multi-standard receivers,” *Progress In Electromagnetics Research*, Vol. 129, 421–437, 2012.
 9. Aluigi, L., L. Roselli, S. M. White, and F. Alimenti, “System-on-chip 36.8 GHz radiometer for space-based observation of solar flares: Feasibility study in 0.25 μm SiGe BiCMOS technology,” *Progress In Electromagnetics Research*, Vol. 130, 347–368, 2012.
 10. De la Morena-Álvarez-Palencia, C. and M. Burgos-Garcia, “Four-octave six-port receiver and its calibration for broadband communications and software defined radios,” *Progress In Electromagnetics Research*, Vol. 116, 1–21, 2011.
 11. Moscoso-Martir, A., I. Molina-Fernandez, and A. Ortega-Monux, “Signal constellation distortion and BER degradation due to hardware impairments in six-port receivers with analog I/Q generation,” *Progress In Electromagnetics Research*, Vol. 121, 225–247, 2011.
 12. Bonafoni, S., F. Alimenti, G. Angelucci, and G. Tasselli, “Microwave radiometry imaging for forest fire detection: A simulation study,” *Progress In Electromagnetics Research*, Vol. 112, 77–92, 2011.
 13. Asimakis, N. P., I. S. Karanasiou, and N. K. Uzunoglu, “Non-invasive microwave radiometric system for intracranial applications: A study using the conformal L-notch microstrip patch antenna,” *Progress In Electromagnetics Research*, Vol. 117, 83–101, 2011.
 14. Giamalaki, M. I. and I. S. Karanasiou, “Enhancement of a microwave radiometry imaging system’s performance using left handed materials,” *Progress In Electromagnetics Research*, Vol. 117, 253–265, 2011.
 15. Kim, W.-G., N.-W. Moon, J. Kang, and Y.-H. Kim, “Loss measuring of large aperture quasi-optics for W-band imaging radiometer system,” *Progress In Electromagnetics Research*, Vol. 125, 295–309, 2012.
 16. D’Orazio, A., et al., “Optimisation of tipping curve calibration of microwave radiometer,” *Electronics Letters*, Vol. 39, No. 12, 905–906, Jun. 2003.

17. Han, Y., et al., "Analysis and improvement of tipping calibration for ground-based microwave radiometers," *IEEE Trans. on Geosci. Remote Sens.*, Vol. 38, No. 3, 1260–1276, May 2000.
18. Liebe, H. J., et al., "Propagation modeling of moist air and suspended waterice particles at frequencies below 1000 GHz," *Atmospheric Propagation Effects through Natural and Manmade Obscurants for Visible to mm-wave Radiation*, Palma De Mallorca, Spain, May 1993.
19. Hewison, T. J., "1D-VAR retrieval of temperature and humidity profiles from a ground-based microwave radiometer," *IEEE Trans. on Geosci. Remote Sens.*, Vol. 45, No. 7, 2163–2168, Jul. 2007.
20. Hewison, T. J., "Profiling temperature and humidity by ground-based microwave radiometers," Ph. D. Dissertation, The University of Reading, Whiteknights, United Kingdom, 2006.
21. Scheve, T. M. and C. T. Swift, "Profiling atmospheric water vapor with a K-band spectral radiometer," *IEEE Trans. on Geosci. Remote Sens.*, Vol. 37, No. 3, Part 2, 1719–1729, May 1999.
22. Chang, L., H. Zhou, L.-L. Chen, X.-Z. Xiong, and C. Liao, "The fine-grained parallel micro-genetic algorithm and its application to broadband conical corrugated-horn antenna," *Progress In Electromagnetics Research*, Vol. 138, 599–611, 2013.
23. Chen, C.-Y. and C.-C. Lin, "The design and fabrication of a highly compact microstrip dual-band bandpass filter," *Progress In Electromagnetics Research*, Vol. 112, 299–307, 2011.
24. Rezaee, P., M. Tayarani, and R. Knöchel, "Active learning method for the determination of coupling factor and external Q in microstrip filter design," *Progress In Electromagnetics Research*, Vol. 120, 459–479, 2011.
25. Yang, B., G. Mehdi, A. Hu, Y. Xie, X. Yao, J. Zhang, C. Zheng, and J. Miao, "The round-ended design and measurement of all symmetric edge-coupled bandpass filter," *Progress In Electromagnetics Research C*, Vol. 38, 191–203, 2013.
26. Chang, L., C. Liao, L.-L. Chen, W. Lin, X. Zheng, and Y.-L. Wu, "Design of an ultra-wideband power divider via the coarse-grained parallel micro-genetic algorithm," *Progress In Electromagnetics Research*, Vol. 124, 425–440, 2012.
27. Wang, D., H. Zhang, T. Xu, H. Wang, and G. Zhang, "Design and optimization of equal split broadband microstrip Wilkinson power divider using enhanced particle swarm optimization algorithm," *Progress In Electromagnetics Research*, Vol. 118, 321–334, 2011.
28. Li, B., X. Wu, N. Yang, and W. Wu, "Dual-band equal/unequal

- Wilkinson power dividers based on coupled-line section with short-circuited stub,” *Progress In Electromagnetics Research*, Vol. 111, 163–178, 2011.
29. Amaduzzi, L. and M. Tinti, “Low cost components radiometer implementation for human microwave electromagnetic field emission detection,” *Progress In Electromagnetics Research Letters*, Vol. 23, 9–18, 2011.
 30. Midford, T. A., J. J. Wooldridge, and R. L. Sturdivant, “The evolution of packages for monolithic microwave and millimeter-wave circuits,” *IEEE Trans. on Antennas and Propag.*, Vol. 43, No. 9, 983–991, Sep. 1995.
 31. Wein, D. S., “Advanced ceramic packaging for microwave and millimeter wave applications,” *IEEE Trans. on Antennas and Propag.*, Vol. 43, No. 9, 940–948, Sep. 1995.
 32. Klemetsen, O., Y. Birkelund, S. K. Jacobsen, P. F. Maccarini, and P. R. Stauffer, “Design of medical radiometer front-end for improved performance,” *Progress In Electromagnetics Research B*, Vol. 27, 289–306, 2011.
 33. Ulaby, F. T., et al., *Microwave Remote Sensing: Active and Passive, Volume I: Fundamentals and Radiometry*, Artech House Publishers, Mar. 1986.
 34. Iturbide-Sanchez, F. and S. Padmanabhan, “A miniaturized spectrometer radiometer based on MMIC technology for tropospheric water vapor profiling,” *IEEE Trans. on Geosci. Remote Sens.*, Vol. 45, No. 7, 2181–2194, Jul. 2007.
 35. Janssen, M. A., “An introduction to the passive microwave remote sensing of atmospheres,” *Atmospheric Remote Sensing by Microwave Radiometry*, M. A. Janssen (ed.), 1–35, Wiley, New York, 1993.
 36. Schneebeli, M. and C. Mätzler, “A calibration scheme for microwave radiometers using tipping curves and Kalman filtering,” *IEEE Trans. on Geosci. Remote Sens.*, Vol. 47, No. 12, 4201–4209, Dec. 2009.